nature chemistry

Article

https://doi.org/10.1038/s41557-024-01569-y

Hydrogen splitting at a single phosphorus centre and its use for hydrogenation

Received: 26 July 2023

Accepted: 30 May 2024

Published online: 27 June 2024

Check for updates

Deependra Bawari[1,2], Donia Toami[1,2], Kuldeep Jaiswal[1,2] & Roman Dobrovetsky[1]

Catalytic processes are largely dominated by transition-metal complexes. Main-group compounds that can mimic the behaviour of the transition-metal complexes are of great interest due to their potential to substitute or complement transition metals in catalysis. While a few main-group molecular centres were shown to activate dihydrogen via the oxidative addition process, catalytic hydrogenation using these species has remained challenging. Here we report the synthesis, isolation and full characterization of the geometrically constrained phosphenium cation with the 2,6-bis(*o*-carborano)pyridine pincer-type ligand. Notably, this cation can activate the H–H bond by oxidative addition to a single P^{III} cationic centre, producing a dihydrophosphonium cation. This phosphenium cation is also capable of catalysing hydrogenation reactions of C=C double bonds and fused aromatic systems, making it a main-group compound that can both activate H_2 at a single molecular main-group centre and be used for catalytic hydrogenation. This finding shows the potential of main-group compounds, in particular phosphorus-based compounds, to serve as metallomimetic hydrogenation catalysts.

Main-group compounds capable of mimicking transition-metal reactivity in the activation of small molecules, such as dihydrogen, attract much interest from the scientific community due to their potential to serve as alternatives to noble transition-metal catalysts[1–3]. The basic principle for the design of main-group compounds capable of activating small molecules at a single main-group centre is that they have to possess a high-lying highest occupied molecular orbital (HOMO) and a low-lying lowest unoccupied molecular orbital (LUMO). This was achieved in certain low-valent compounds such as carbenes[3–5], borylenes[6–9] and their heavier analogues[2,10–14]. Alternatively, two main-group centres in the bimolecular or unimolecular system, in which one centre is a strong Lewis base (high HOMO) and the other is a strong Lewis acid (low LUMO) known as frustrated Lewis pairs were also shown to activate small molecules between these two centres[15,16]. Recently, the activation of small molecules by phosphorus-based species gained a lot of attention due to their ability to cycle between two stable oxidation states P^{III} and P^{V} (refs. 17,18). The strategy to obtain an ambiphilic (both nucleophilic and electrophilic) P^{III} centre, which can activate small molecules, is to geometrically constrain it by a rigid pincer-type ligand[17,18]. This constraint causes the rehybridization of the molecular orbitals (MOs) at the P centre and as a result a decrease in the HOMO–LUMO gap[17,18]. Ambiphilic, geometrically constrained P^{III} centres were shown to activate O–H (refs. 19–22), N–H (refs. 23–25), Ar–F (refs. 26,27) and Si–H (ref. 28) bonds by their formal oxidative addition, producing new P^{V} species. In some cases, these activation processes were reversible and the initial P^{III} compounds could be obtained back as a result of the reductive elimination-type reaction[23–25]. Despite recent progress in the activation of small molecules at the ambiphilic P^{III} centres and participation of some P centres in the activation of H_2 (refs. 29–33), a highly desirable activation of the H–H bond by a formal oxidative addition to the P^{III} centre was never reported. In fact, only recently an example of the oxidative addition of H_2 to presumably transient stibinidene, formed from distibene, was reported[34], which until now is the only Group 15 molecular centre capable of such reactivity. Furthermore, while the activation of the H–H bond by a few ambiphilic single main-group centres was shown[2–14], catalytic hydrogenation using these species was never reported.

[1]School of Chemistry, Raymond and Beverly Sackler Faculty of Exact Sciences, Tel Aviv University, Tel Aviv, Israel. [2]These authors contributed equally: Deependra Bawari, Donia Toami, Kuldeep Jaiswal. e-mail: rdobrove@tau.ac.il

https://doi.org/10.1038/s41557-024-01569-y

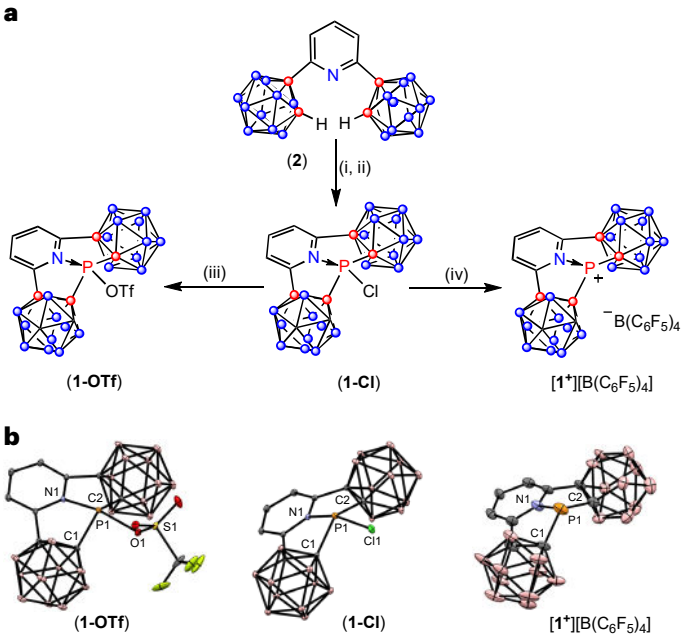

Fig. 1 | Synthesis and structures of 1-Cl, 1-OTf and [1^{+}][B(C$_6$F$_5$)$_4$]. a, The synthesis of **1-Cl**, **1-OTf** and [**1**$^{+}$][B(C$_6$F$_5$)$_4$]. Reaction conditions: (i) 2.3 equiv. ^{n}BuLi, 0 °C, Et$_2$O, 2 days stirring at RT; (ii) 10 equiv. PCl$_3$, −20 °C, C$_6$H$_6$, 18 h reflux at 110 °C; (iii) AgOTf, CH$_2$Cl$_2$, 12 h stirring at RT; (iv) [Et$_3$Si][B(C$_6$F$_5$)$_4$], toluene, 20 h stirring at RT. **b**, Persistence of Vision Raytracer (POV-ray) depictions of **1-OTf** (left), **1-Cl** (centre) and **1**$^{+}$ (right), thermal ellipsoids at the 30% probability level, hydrogens and [B(C$_6$F$_5$)$_4$]$^{-}$ were omitted for clarity.

In this Article, we report the synthesis, isolation and full characterization of the ambiphilic, geometrically constrained phosphenium cation (**1**$^{+}$) (Fig. 1). The reaction of **1**$^{+}$ with dihydrogen produces the dihydrophosphonium cation (**1**$^{+}$**-H$_2$**) via a formal oxidative addition of H−H bond to P^{III} centre in **1**$^{+}$ (Fig. 3). Experimental studies and density functional theory (DFT) calculations of the possible mechanism of this activation (Fig. 3), as well as the use of **1**$^{+}$ in the catalytic hydrogenation reactions of C=C double bonds and fused aromatic systems, are also described (Fig. 4).

Results and discussion

To design a molecule with a highly reactive, ambiphilic P^{III} cationic centre, a pincer-type ligand bearing two *ortho*-carborane (*o*Cb) 'arms' and a neutral central pyridine donor (**2**) was chosen (Fig. 1a)[35]. We envisioned that **2** would provide the necessary rigidity and robustness to structurally constrain the P^{III} cationic centre, the pyridine donor would stabilize this cationic centre, while the strongly electron-withdrawing *o*Cb 'arms'[36–38] would make this P^{III} centre highly electrophilic (low-lying LUMO). Thus, **2** was doubly deprotonated by ^{n}BuLi and reacted with an excess of PCl$_3$ (10 equiv.) producing chlorophosphine **1-Cl** (Fig. 1a). Colourless crystals of **1-Cl** were obtained from a mixture of CH$_2$Cl$_2$/*n*-hexane (10:1) and measured using X-ray crystallography (Fig. 1b). In an attempt to obtain the desired **1**$^{+}$, **1-Cl** was reacted with AgOTf (1 equiv.); however, instead of a separated [**1**$^{+}$][OTf] ion pair, **1-OTf** was obtained (Fig. 1a). The **1-OTf** was crystallized from CH$_2$Cl$_2$ at room temperature (RT), and its X-ray molecular structure is shown in Fig. 1b. The ^{31}P nuclear magnetic resonance (NMR) chemical shift of **1-OTf** at δ = 36.0 ppm resembles the chemical shift of **1-Cl** (δ = 33.8 ppm), indicating that, despite the *trans* influence from the pyridine donor, no dissociation to **1**$^{+}$ and TfO^{-} occurs in solution at RT on the NMR timescale. This points to the highly electrophilic P^{III} centre in **1-OTf**. To obtain a non-coordinated, 'free' **1**$^{+}$ cation, the chloride in **1-Cl** was abstracted by [Et$_3$Si][B(C$_6$F$_5$)$_4$], giving the desired [**1**$^{+}$][B(C$_6$F$_5$)$_4$] (Fig. 1a). The [**1**$^{+}$][B(C$_6$F$_5$)$_4$] was crystallized from CHCl$_3$ as light-yellow crystals and its molecular structure was determined by X-ray crystallography (Fig. 1b). The [**1**$^{+}$][B(C$_6$F$_5$)$_4$] is a separated ion pair both in solid and solution with a low-field signal in ^{31}P NMR at δ = 132.2 ppm. The P centre in **1**$^{+}$ is pyramidalized and strongly deviated from a local C_{3v} symmetry, which is typical to trigonal pyramidal σ^3P centres, with bond angles around phosphorus atom being ∠C1–P1–C2 = 124.1°, ∠N1–P1–C1 and ∠N1–P1–C2 = 87.2°. Thus, ligand **2** enforces a distorted trigonal pyramidal geometry of the P1 centre in **1**$^{+}$ with a C_s local symmetry, which could be described as a *cis*-divacant pseudo trigonal bipyramid in which C1 and C2 atoms of the *o*Cb units are at the equatorial positions and the central N1 is at the axial one.

The electronic structure of **1**$^{+}$ was studied by DFT calculations performed at the BP86(D3)/def2-TZVP level of theory[39–43]. The optimized geometry of **1**$^{+}$ is in good agreement with the experimentally obtained structure (Fig. 1b). The MO analysis of **1**$^{+}$ reveals that the HOMO is primarily located on the P centre, while the LUMO is located on the P centre with the expected delocalization into the pyridine π-system, with the calculated HOMO–LUMO energy gap of 2.8 eV (Fig. 2a). The natural bond orbital analysis shows that the lone pair at the P centre (occupancy of 1.85 e) resides on an sp$^{0.87}$ hybrid with a dominant *s* character. The natural population analysis exhibits charges of −0.47 and +1.26 on N and P centres, respectively. An electron occupancy of the N1–P1 bond of 1.53 e was calculated, with the bonding coefficients substantially polarized towards the N1 centre (92.76% and 7.24% on N1 and P1, respectively). The calculated Wiberg bond index value for N1–P1 bond is 0.64. The nature of the N–P bond in **1**$^{+}$ was also analysed by Bader's quantum theory of atoms in molecules (AIM)[44]. A positive Laplacian ($\nabla^2\rho(r_{BCP})$ = 0.075159), low magnitude of electron density (ρ = 0.136520), the values of $H_b/\rho(r)$ (−0.802680) < 0, $G(r)/\rho(r)$ (0.940316) ~ 1.0 and $G(r)$«$|V(r)|$ at the bond critical point (BCP) of the N–P bond in **1**$^{+}$ indicate the donor–acceptor interactions between these two atoms (Fig. 2b). Considering all these factors, the nature of **1**$^{+}$ can be most accurately described as a pyridine-supported phosphenium cation.

The small HOMO–LUMO gap (2.8 eV) in **1**$^{+}$ suggests a high reactivity of this P^{III} centre, which encouraged us to check its reactivity with H$_2$. Thus, a J-Young NMR tube containing CHCl$_3$ solution of [**1**$^{+}$][B(C$_6$F$_5$)$_4$] was pressurized with H$_2$ (4 atm), and the reaction was left at RT while the reaction progress was monitored by multi-nuclear NMR spectroscopy. After ~7 days, the formation of [**1**$^{+}$**-H$_2$**][B(C$_6$F$_5$)$_4$] (ca. 15–20%), the formal oxidative addition product of the H–H bond to the P^{III} cationic centre in **1**$^{+}$ (Fig. 3a), could be observed by the ^{31}P NMR as a triplet at δ = −42.66 ppm with ^{1}J(PH) of 504 Hz (Fig. 3b). The corresponding doublet with same coupling constant was measured by ^{1}H NMR at δ = 7.35 ppm (^{1}J(PH) = 504 Hz). The reaction time could be considerably reduced (18 h) by heating the reaction to 50 °C. Prolonged heating at temperatures of 50 °C or higher led to the formation of a more complex mixture, where notable amounts of unidentified byproducts were also formed alongside the [**1**$^{+}$**-H$_2$**][B(C$_6$F$_5$)$_4$]. The [**1**$^{+}$**-H$_2$**][B(C$_6$F$_5$)$_4$] was crystallized from CH$_2$Cl$_2$/toluene solution (3:1) as colourless crystals and its molecular structure was determined using X-ray crystallography (Fig. 3c). In the solid state, the P centre in **1**$^{+}$**-H$_2$** has a slightly distorted square pyramidal (SP) geometry with bond angles around phosphorus atom being ∠N1–P1–H2 = 163.5°, ∠N1–P1–H1 = 89.1°, ∠C1–P1–C2 143.1° and with P1–H1 and P1–H2 bond lengths of 1.19 and 1.39 Å, respectively. Interestingly, unlike the solid-state structure of **1**$^{+}$**-H$_2$** with two different H atoms attached to the P centre, in the solution of [**1**$^{+}$**-H$_2$**][B(C$_6$F$_5$)$_4$] only one type of H atom attached to the P centre is observed by ^{31}P and ^{1}H NMR in the range of 50 to −50 °C (Supplementary Figs. 54–55), which can be explained by the fast isomerization between the two SP isomers. This was also supported by the low DFT calculated (BP86(D3)/def2-TZVP[39–43] in CHCl$_3$ using the conductor-like polarizable continuum model (CPCM)[45,46]) activation barrier of $\Delta G^{\ddagger}$ = 2.6 kcal mol^{-1} of this isomerization process (Supplementary Fig. 53).

To study this activation process, the reaction of [**1**$^{+}$][B(C$_6$F$_5$)$_4$] with hydrogen deuteride (HD) gas was performed. As a result, no HD scrambling to H$_2$ and D$_2$ was observed by ^{1}H NMR, and only the triplet (4.58 ppm J_{HD} = 43 Hz) associated with HD was detected (Supplementary Fig. 58).

https://doi.org/10.1038/s41557-024-01569-y

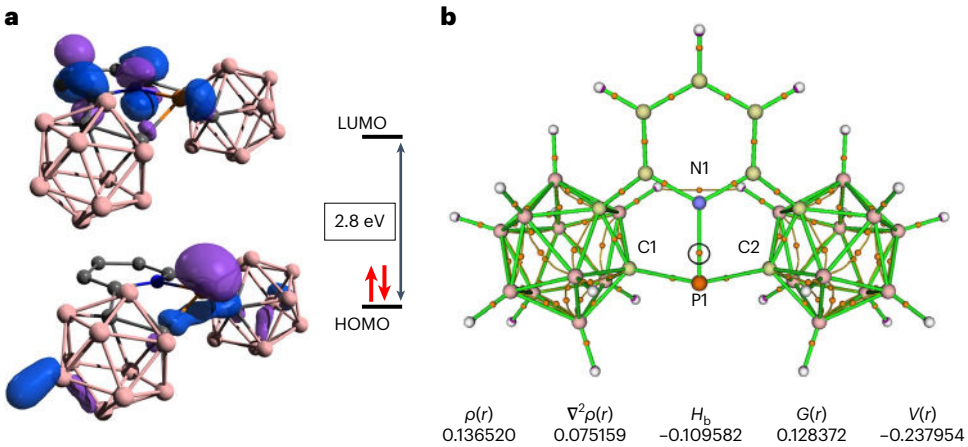

Fig. 2 | Electronic structure of 1^+. a, DFT-calculated FMOs (isovalue of 0.05) and the HOMO–LUMO gap in 1^+. **b**, Atoms in molecules (AIM) analysis of 1^+; the values of electron density (ρ), Laplacian of electron density (∇^2_ρ), total energy density (H_b), kinetic-energy density (G) and potential energy density (V) at the P–N bond critical point (circled) are shown below the structure.

The formation of [**1**$^+$**-HD**][$B(C_6F_5)_4$] was confirmed by the appearance of a doublet of triplet at −42.9 ppm (J_{P-H} = 495 Hz, J_{P-D} = 81 Hz) in the ^{31}P NMR spectrum (Supplementary Figs. 59 and 60). The failure to release H_2 from [**1**$^+$**-H$_2$**][$B(C_6F_5)_4$] by heating it under vacuum indicated that the H_2 activation by [**1**$^+$][$B(C_6F_5)_4$] is irreversible.

Next, the pseudo-first-order kinetic studies were conducted on the activation of H_2 by [**1**$^+$][$B(C_6F_5)_4$]. An NMR tube was charged with [**1**$^+$][$B(C_6F_5)_4$] in $CHCl_3$ and H_2 gas was introduced. The reaction progress was monitored by NMR, with the concentration of [H_2] in solution determined from the ^{1}H NMR signal (4.61 ppm), assuming 25% of the H_2 is parahydrogen.[47] NMR measurements showed that the [H_2] remained constant throughout the reaction, while the amount of H_2 in the NMR tube exceeded that of [**1**$^+$][$B(C_6F_5)_4$] by at least tenfold, enabling the determination of the pseudo-first-order rate for the consumption of [**1**$^+$][$B(C_6F_5)_4$]. Consequently, the pseudo-first-order behaviour in [**1**$^+$][$B(C_6F_5)_4$] is evidenced by the fact that every reaction profile can be fitted to a pseudo-first-order plot (Supplementary Fig. 67). Subsequently, the order in [H_2] was elucidated by varying the pressure of H_2 between 1 and 4 atm. The observed rate constant (k_{obs}) exhibited a direct proportionality to [H_2]. The ln[k_{obs}]-versus-ln[H_2] plot yielded a slope of 0.97 (Supplementary Fig. 68), indicating the order in [H_2] to be 1. Thus, the obtained results are consistent with the second-order formation of the [**1**$^+$**-H$_2$**][$B(C_6F_5)_4$].

On the basis of these experiments, we suggest that the activation of the H–D (and the H–H) bond most probably occurs at a single P^{III} centre via an oxidative addition type reaction. To the best of our knowledge, the oxidative addition of an H–H bond to a single, well-defined phosphorus centre has not yet been reported.

To get a deeper insight into the mechanism of H_2 activation by **1**$^+$, DFT computations were carried out at the previously used level of theory (vide supra) in $CHCl_3$ using the CPCM[45,46]. These calculations show that the oxidative addition of the H–H bond to P^{III} centre in **1**$^+$ producing **1**$^+$**-H$_2$** is both exothermic and exergonic (ΔH = −16.4 and ΔG = −7.8 kcal mol^{-1}) (Fig. 3d). The Gibbs free energy barrier of $\Delta G^{\ddagger}$ = 32.5 kcal mol^{-1} (transition state (**TS**)) of this H_2 activation reaction is reasonable and can explain long reaction times and/or heating requirements. Importantly, alternative modes of H_2 activation, including those involving the pyridinyl moiety were also considered; however, calculations showed that all of these pathways are notably higher in energy (Supplementary Figs. 57 and 65–66). The geometry of the (**TS**) suggests that this activation is most probably an electrophilically driven process, as the H–H σ bond approaches the P centre from the direction in which the LUMO points (Fig. 3d and Supplementary Fig. 70). The frontier molecular orbital (FMO) analysis[48] of **1**$^+$ and H_2, revealing a small energy gap of 5.05 eV between the LUMO of **1**$^+$ and the HOMO of H_2 compared with the large energy gap (9.62 eV) between the HOMO of **1**$^+$ and the LUMO of H_2 (Supplementary Fig. 69), suggests the electrophilically dominated nature of this reaction.

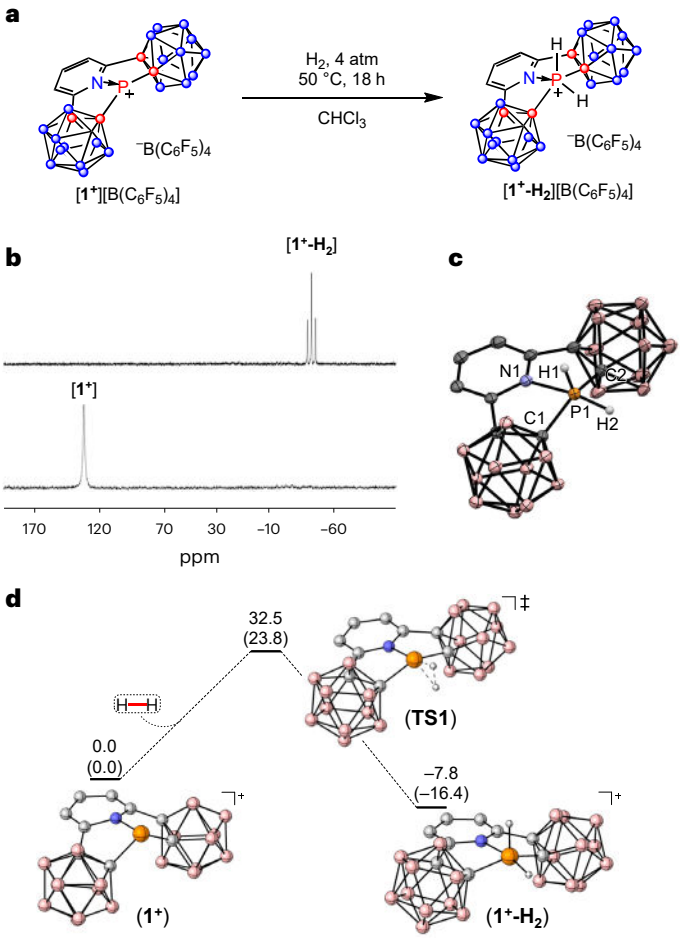

Fig. 3 | Activation of H_2 by 1^+. a, Formal oxidative addition of H–H bond to P^{III} cationic centre in 1^+. **b**, Stacked ^{31}P NMR spectra showing the formation of [**1**$^+$**-H$_2$**] from [**1**$^+$] and H_2. **c**, POV-ray depiction of [**1**$^+$**-H$_2$**], thermal ellipsoids at the 30% probability level, non-relevant hydrogens and $[B(C_6F_5)_4]^-$ were omitted for clarity. **d**, DFT-calculated mechanism for the activation of H_2 by **1**$^+$. Free Gibbs energies (enthalpies) are given relative to the starting materials.

https://doi.org/10.1038/s41557-024-01569-y

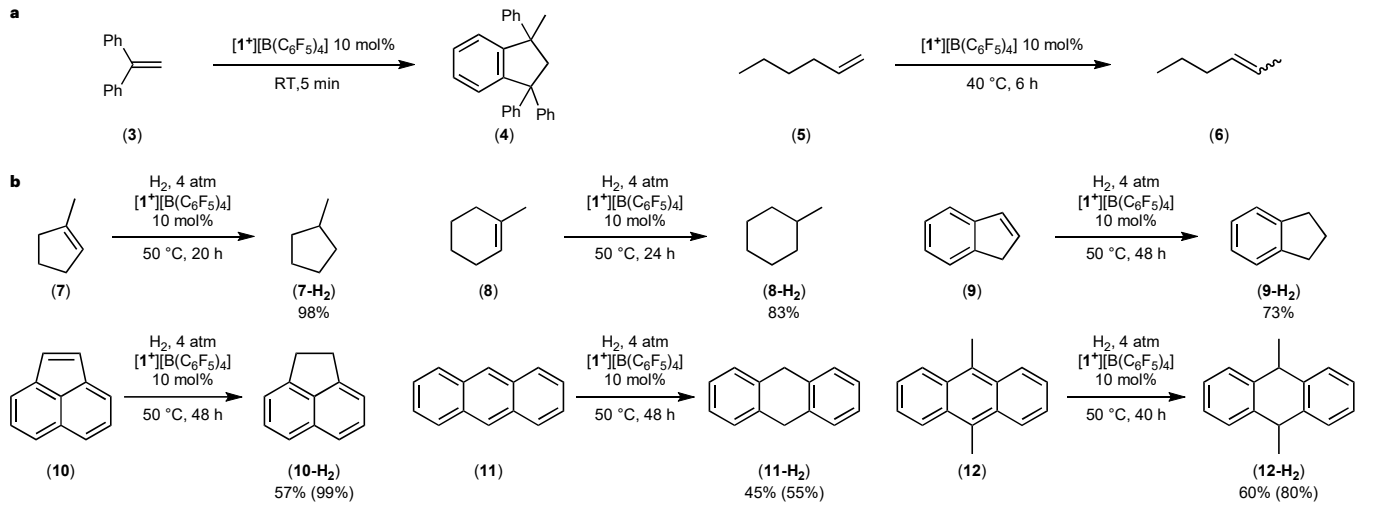

Fig. 4 | Catalysis with [1⁺][B(C$_6$F$_5$)$_4$]. **a**, The [1⁺][B(C$_6$F$_5$)$_4$] catalysed dimerization and isomerization reactions. **b**, The [1⁺][B(C$_6$F$_5$)$_4$] catalysed hydrogenation reactions of unsaturated C–C systems (gas chromatography or isolated yields (NMR yields)).

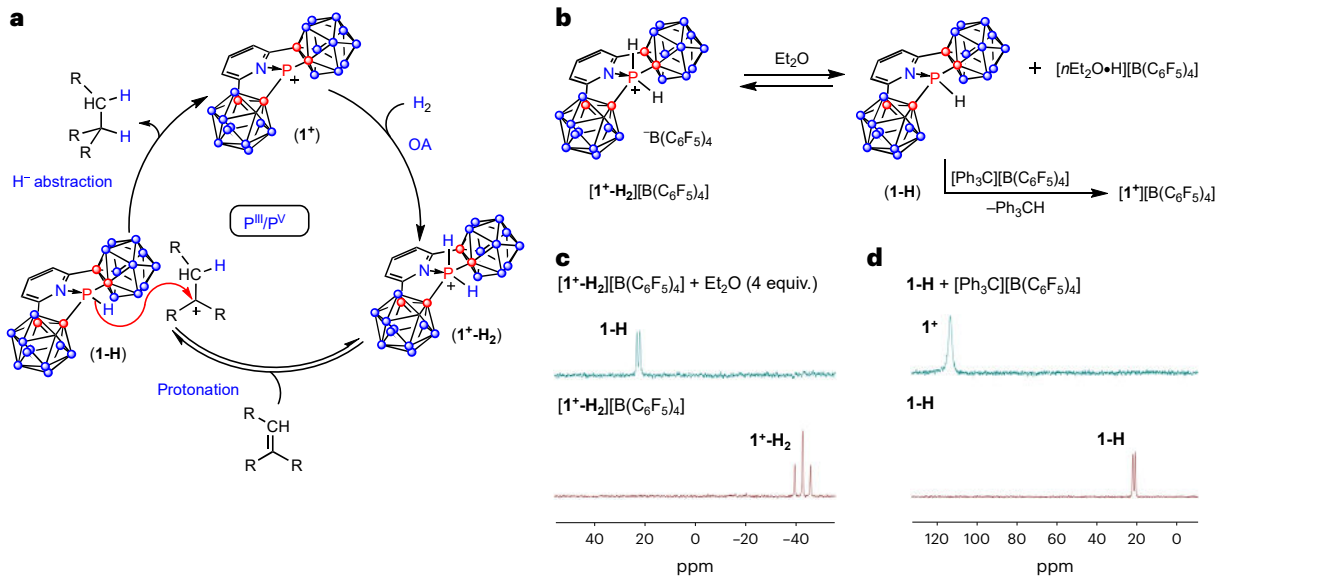

Fig. 5 | Mechanism of the catalysis. **a**, The proposed catalytic cycle for the hydrogenation of C=C doubly bonded system catalysed by [1⁺]. OA, oxidative addition. **b**, Experimental support for the protonation (reaction with Et$_2$O) and hydride abstraction (reaction with [Ph$_3$C][B(C$_6$F$_5$)$_4$]) steps of the proposed catalytic cycle. **c**, ^{31}P NMR of the reaction of [1⁺-H$_2$][B(C$_6$F$_5$)$_4$] with Et$_2$O. **d**, ^{31}P NMR of the reaction of 1-H with [Ph$_3$C][B(C$_6$F$_5$)$_4$].

The ability of 1⁺ to transfer hydrogen catalytically was tested with various unsaturated C–C bond-containing systems. First, the reaction of highly active terminal alkene, 1,1-diphenylethylene (**3**) with H$_2$ (4 atm) and 10 mol% of [1⁺][B(C$_6$F$_5$)$_4$] was probed. This reaction, however, led to the 1,1-diphenylethylene dimerization product (**4**) in minutes (~5 min) at RT[49], while the desired 1,1-diphenylethane, a hydrogenation product, was not obtained. A similar reaction was conducted with 1-hexene (**5**), H$_2$ (4 atm) and [1⁺][B(C$_6$F$_5$)$_4$] (10 mol%) at 40 °C, affording mostly isomerization product (**6**)[49] after 6 h, and again no hydrogenation of the C=C double bond occurred even after prolonged heating. Importantly, both reactions of **3** and **5** in the presence of 10 mol% of [1⁺][B(C$_6$F$_5$)$_4$] without the addition of H$_2$ gave the same results, that is, formation of **4** and **6**, respectively (Fig. 4a). Therefore, the dimerization of **3** as well as isomerization of **5** are catalysed by 1⁺, indicating once again the high Lewis acidity of this cation[49].

To overcome this obstacle, the unsaturated C–C bond-containing systems that are not capable of isomerization, dimerization or polymerization, which preclude the desired hydrogenation, were tested next. Thus, a reaction of 1-methylcyclopentene (**7**) with H$_2$ (4 atm) in the presence of 10 mol% of [1⁺][B(C$_6$F$_5$)$_4$] gave after 20 h at 50 °C quantitative formation of the hydrogenated product, methylcyclopentane (**7-H$_2$**) (Fig. 4b). A similar reaction with 1-methylcyclohexene (**8**) at 50 °C, after 24 h afforded the corresponding hydrogenated product, methylcyclohexane (**8-H$_2$**) in high yields (Fig. 4b). The hydrogenation (H$_2$, 4 atm) of indene (**9**) and acenaphthylene (**10**) catalysed by [1⁺][B(C$_6$F$_5$)$_4$] (10 mol%) was also successful, leading to indane (**9-H$_2$**) and acenaphthene (**10-H$_2$**), respectively, after 48 h at 50 °C (Fig. 4b). The hydrogenation of fused aromatic systems anthracene (**11**) and 9,10-dimethylanthracene (**12**) was also attempted. Thus, the reaction of **11** with H$_2$ (4 atm) and [1⁺][B(C$_6$F$_5$)$_4$] (10 mol%) at 50 °C afforded after 48 h 9,10-dihydroanthracene (**11-H$_2$**). A similar result was obtained for the [1⁺][B(C$_6$F$_5$)$_4$] (10 mol%) catalysed hydrogenation (H$_2$, 4 atm) of **12**, producing **12-H$_2$** after 40 h at 50 °C (Fig. 4b). Remarkably, 1⁺ is capable of splitting H$_2$ at a single main-group centre and transfer it catalytically to unsaturated C–C bonds.

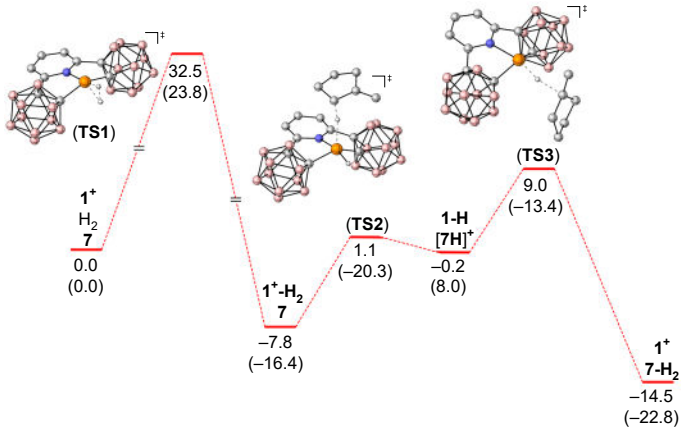

Fig. 6 | Computed hydrogenation mechanism. DFT-calculated PES for the hydrogenation of methylcyclopentene (**7**) at the BP86(D3)/def2-TZVP level of theory with CPCM($CHCl_3$). Free Gibbs energies (enthalpies) (in kcal mol^{-1}) are given relative to the starting materials.

To gain a deeper understanding of the catalytic hydrogenation process, [**1**$^+$-**H$_2$**][$B(C_6F_5)_4$] was reacted with 10 equiv. of **11**, which at RT instantly resulted in the formation of **1-H** and [**1**$^+$-**H$_2$**][$B(C_6F_5)_4$] mixture (1:0.7 ratio, respectively), as determined by ^{31}P NMR (Supplementary Fig. 74). To confirm the formation of **1-H**, it was independently prepared by the reaction of **1-Cl** with diisobutylaluminium hydride (Supplementary Figs. 23–29). Heating this mixture to 50 °C for 3 h yielded **11-H$_2$** (Supplementary Fig. 75). On the basis of these results, we propose a plausible mechanism for the [**1**$^+$][$B(C_6F_5)_4$] catalysed hydrogenation of the C=C doubly bonded and fused aromatic systems. The catalysis begins with the activation of H_2 to produce [**1**$^+$-**H$_2$**][$B(C_6F_5)_4$]. Subsequently, an equilibrium process in which the deprotonation of [**1**$^+$-**H$_2$**][$B(C_6F_5)_4$] by the unsaturated carbon system occurs producing **1-H** and the corresponding carbocation (Supplementary Fig. 73). Finally, in the last step of the catalysis, the carbocation abstracts the hydride from **1-H**, leading to the hydrogenated product and regeneration of the catalyst [**1**$^+$][$B(C_6F_5)_4$] (Fig. 5a).

To further support this mechanism, the high acidity of [**1**$^+$-**H$_2$**][$B(C_6F_5)_4$] was investigated compared with Et_2O. The gradual addition of Et_2O to [**1**$^+$-**H$_2$**][$B(C_6F_5)_4$] at RT and monitoring of the reaction mixture by ^{31}P NMR revealed an equilibrium between [**1**$^+$-**H$_2$**][$B(C_6F_5)_4$], Et_2O and **1-H**, [*n*Et_2O·H][$B(C_6F_5)_4$] (Fig. 5b,c). This observation suggests that the Bronsted acidity of [**1**$^+$-**H$_2$**][$B(C_6F_5)_4$] is comparable to that of Jutzi's acid[50]. Additionally, **1-H** was reacted with [Ph_3C][$B(C_6F_5)_4$], resulting in the formation of [**1**$^+$][$B(C_6F_5)_4$] and Ph_3CH (Fig. 5b,d), demonstrating the ability of **1-H** to act as a hydride donor.

Finally, the potential energy surface (PES) for the proposed mechanism was calculated for the catalytic hydrogenation of **7** (Fig. 6) (see Supplementary Information for the PES for the catalytic hydrogenation of **11**) at the previously used level of theory (vide supra) in $CHCl_3$ using CPCM. The first step, which is the activation of H_2 by **1**$^+$ leading to **1**$^+$-**H$_2$**, as was shown previously, is exergonic and exothermic with the activation Gibbs free energy of 32.5 kcal mol^{-1} (**TS1**). The protonation step of **7** leading to **1-H** and **7-H**$^+$ is endergonic and endothermic (ΔG = 7.6 and ΔH = 24.4 kcal mol^{-1}), with the activation barrier of $\Delta G^{\ddagger}$ = 8.9 (**TS2**). The next step, which is the abstraction of hydride from **1-H** by **7-H**$^+$ leading to the hydrogenation product **7-H$_2$** (Fig. 6), is also exergonic and exothermic (ΔG = −14.3 and ΔH = −30.8 kcal mol^{-1}). The activation energy of the hydride abstraction step is $\Delta G^{\ddagger}$ = 9.2 (**TS3**). Based on this PES, the rate-determining step in this catalysis is the H_2 activation by **1**$^+$.

In summary, we have synthesized an ambiphilic, geometrically constrained phosphenium cation with a pincer-type ligand that is capable of activating H_2 in a metallomimetic fashion by formal oxidative addition of the H–H bond to the P^{III} cationic centre. Preliminary mechanistic studies suggest that this H_2 splitting, similarly to transition metal-based H_2 activation, is an electrophilically driven process. Notably, the ability of this phosphenium cation to activate H_2 was used for catalytic hydrogenation reactions of C=C doubly bonded and fused aromatic systems. This finding shows the potential of phosphorus and possibly other main-group elements in metallomimetic catalytic hydrogenation reactions.

Online content

Any methods, additional references, Nature Portfolio reporting summaries, source data, extended data, supplementary information, acknowledgements, peer review information; details of author contributions and competing interests; and statements of data and code availability are available at https://doi.org/10.1038/s41557-024-01569-y.

References

1. Power, P. P. Main-group elements as transition metals. *Nature* **463**, 171–177 (2010).
2. Chu, T. & Nikonov, G. I. Oxidative addition and reductive elimination at main-group element centers. *Chem. Rev.* **118**, 3608–3680 (2018).
3. Martin, D., Soleilhavoup, M. & Bertrand, G. Stable singlet carbenes as mimics for transition metal centers. *Chem. Sci.* **2**, 389–399 (2011).
4. Frey, G. D., Lavallo, V., Donnadieu, B., Schoeller, W. W. & Bertrand, G. Facile splitting of hydrogen and ammonia by nucleophilic activation at a single carbon center. *Science* **316**, 439–441 (2007).
5. Nesterov, V. et al. NHCs in main group chemistry. *Chem. Rev.* **118**, 9678–9842 (2018).
6. Légaré, M.-A. et al. Nitrogen fixation and reduction at boron. *Science* **359**, 896–900 (2018).
7. Dahcheh, F., Martin, D., Stephan, D. W. & Bertrand, G. Synthesis and reactivity of a CAAC–aminoborylene adduct: a hetero-allene or an organoboron isoelectronic with singlet carbenes. *Angew. Chem. Int. Ed.* **53**, 13159–13163 (2014).
8. Soleilhavoup, M. & Bertrand, G. Borylenes: an emerging class of compounds. *Angew. Chem. Int. Ed.* **56**, 10282–10292 (2017).
9. Légaré, M.-A., Pranckevicius, C. & Braunschweig, H. Metallomimetic chemistry of boron. *Chem. Rev.* **119**, 823–8261 (2019).
10. Hicks, J., Vasko, P., Goicoechea, J. M. & Aldridge, S. Synthesis, structure and reaction chemistry of a nucleophilic aluminyl anion. *Nature* **557**, 92–95 (2018).
11. Hicks, J., Vasko, P., Goicoechea, J. M. & Aldridge, S. The aluminyl anion: a new generation of aluminium nucleophile. *Angew. Chem. Int. Ed.* **60**, 1702–1713 (2021).
12. Protchenko, A. V. et al. A stable two-coordinate acyclic silylene. *J. Am. Chem. Soc.* **134**, 6500–6503 (2012).
13. Spikes, G. H., Fettinger, J. C. & Power, P. P. Facile activation of dihydrogen by an unsaturated heavier main group compound. *J. Am. Chem. Soc.* **127**, 12232–12233 (2005).
14. Peng, Y., Ellis, B. D., Wang, X. & Power, P. P. Diarylstannylene activation of hydrogen or ammonia with arene elimination. *J. Am. Chem. Soc.* **130**, 12268–12269 (2008).
15. Stephan, D. W. The broadening reach of frustrated Lewis pair chemistry. *Science* **354**, aaf7229 (2016).
16. Stephan, D. W. Frustrated Lewis pairs: from concept to catalysis. *Acc. Chem. Res.* **48**, 306–316 (2015).
17. Lipshultz, J. M., Li, G. & Radosevich, A. T. Main group redox catalysis of organopnictogens: vertical periodic trends and emerging opportunities in group 15. *J. Am. Chem. Soc.* **143**, 1699–1721 (2021).
18. Abbenseth, J. & Goicoechea, J. M. Recent developments in the chemistry of nontrigonal pnictogen pincer compounds: from bonding to catalysis. *Chem. Sci.* **11**, 9728–9740 (2020).
19. Arduengo III, A. J. et al. The synthesis, structure, and chemistry of 10-Pn-3 systems: tricoordinate hypervalent pnictogen compounds. *J. Am. Chem. Soc.* **109**, 627–647 (1987).

20. Dunn, N. L., Ha, M. & Radosevich, A. T. Main group redox catalysis: reversible P^{III}/P^{V} redox cycling at a phosphorus platform. *J. Am. Chem. Soc.* **134**, 11330–11333 (2012).
21. Zhao, W. et al. Reversible intermolecular E–H oxidative addition to a geometrically deformed and structurally dynamic phosphorous triamide. *J. Am. Chem. Soc.* **136**, 17634–17644 (2014).
22. King, A. J., Abbenseth, J. & Goicoechea, J. M. Reactivity of a strictly t-shaped phosphine ligated by an acridane derived NNN pincer ligand. *Chem.Eur. J.* **29**, e202300818 (2023).
23. Abbenseth, J., Townrow, O. P. E. & Goicoechea, J. M. Thermoneutral NH bond activation of ammonia by a geometrically constrained phosphine. *Angew. Chem. Int. Ed.* **60**, 23625–23629 (2021).
24. Volodarsky, S. & Dobrovetsky, R. Ambiphilic geometrically constrained phosphenium cation. *Chem. Commun.* **54**, 6931–6934 (2018).
25. McCarthy, S. M. et al. Intermolecular N–H oxidative addition of ammonia, alkylamines, and arylamines to a planar σ^3-phosphorus compound via an entropy-controlled electrophilic mechanism. *J. Am. Chem. Soc.* **136**, 4640–4650 (2014).
26. Lim, S. & Radosevich, A. T. Round-trip oxidative addition, ligand metathesis, and reductive elimination in a P^{III}/P^{V} synthetic cycle. *J. Am. Chem. Soc.* **142**, 16188–16193 (2020).
27. Chulsky, K., Malahov, I., Bawari, D. & Dobrovetsky, R. Metallomimetic chemistry of a cationic, geometrically constrained phosphine in the catalytic hydrodefluorination and amination of Ar–F bonds. *J. Am. Chem. Soc.* **145**, 3786–3794 (2023).
28. Volodarsky, S., Bawari, D. & Dobrovetsky, R. Dual reactivity of a geometrically constrained phosphenium cation. *Angew. Chem. Int. Ed.* **61**, e202208401 (2022).
29. Zander, E. et al. Rational design of persistent phosphorus-centered singlet tetraradicals and their use in small-molecule activation. *J. Am. Chem. Soc.* **145**, 14484–14497 (2023).
30. Birchall, N., Feil, C. M., Gediga, M., Nieger, M. & Gudat, D. Reversible cooperative dihydrogen binding and transfer with a bis-phosphenium complex of chromium. *Chem. Sci.* **11**, 9571–9576 (2020).
31. Gediga, M., Schlindwein, S. H., Bender, J., Nieger, M. & Gudat, D. Variable reactivity of a N-heterocyclic phosphenium complex: P–C bond activation or 'abnormal' deprotonation. *Angew. Chem. Int. Ed.* **56**, 15718–15722 (2017).
32. Normand, A. T. et al. Phosphido- and amidozirconocene cation-based frustrated Lewis pair chemistry. *J. Am. Chem. Soc.* **137**, 10796–10808 (2015).
33. Hoyle, M.-A. M., Pantazis, D. A., Burton, H. M., McDonald, R. & Rosenberg, L. Benzonitrile adducts of terminal diarylphosphido complexes: preparative sources of 'Ru=PR2'. *Organometallics* **30**, 6458–6465 (2011).
34. Pang, Y., Leutzsch, M., Nöthling, N. & Cornella, J. Dihydrogen and ethylene activation by a sterically distorted distibene. *Angew. Chem. Int. Ed.* **2023**, e202302071 (2023).
35. Anderson, K. P. et al. Improved synthesis of icosahedral carboranes containing exopolyhedral B–C and C–C bonds. *Tetrahedron* **75**, 187–191 (2019).
36. Spokoyny, A. M. New ligand platforms featuring boron-rich clusters as organomimetic substituents. *Pure Appl. Chem.* **85**, 903–919 (2013).
37. Fisher, S. P. et al. Nonclassical applications of closo-carborane anions: from main group chemistry and catalysis to energy storage. *Chem. Rev.* **119**, 8262–8290 (2019).
38. Xie, Z. Cyclopentadienyl–carboranyl hybrid compounds: a new class of versatile ligands for organometallic chemistry. *Acc. Chem. Res.* **36**, 1–9 (2003).
39. Perdew, J. P. Density-functional approximation for the correlation energy of the inhomogeneous electron gas. *Phys. Rev. B* **34**, 8822–8824 (1986).
40. Becke, A. D. Density-functional exchange–energy approximation with correct asymptotic behavior. *Phys. Rev. A* **38**, 3098–3100 (1998).
41. Weigend, F. & Ahlrichs, R. Balanced basis sets of split valence, triple zeta valence and quadruple zeta valence quality for H to Rn: design and assessment of accuracy. *Phys. Chem. Chem. Phys.* **7**, 3297–3305 (2005).
42. Grimme, S., Antony, J., Ehrlich, S. & Krieg, H. A consistent and accurate ab initio parametrization of density functional dispersion correction (DFT-D) for the 94 elements H–Pu. *J. Chem. Phys.* **132**, 154104–154119 (2010).
43. Grimme, S., Ehrlich, S. & Goerigk, L. Effect of the damping function in dispersion corrected density functional theory. *J. Comput. Chem.* **32**, 1456–1465 (2011).
44. Bader, R. F. W. *Atoms in Molecules: A Quantum Theory* (Clarendon Press, 1994)
45. Barone, V. & Cossi, M. Quantum calculation of molecular energies and energy gradients in solution by a conductor solvent model. *J. Phys. Chem. A* **102**, 1995–2001 (1998).
46. Cossi, M., Rega, N., Scalmani, G. & Barone, V. Energies, structures, and electronic properties of molecules in solution with the C–PCM solvation model. *J. Comput. Chem.* **24**, 669–681 (2003).
47. Jacobsen, R. T., Leachman, J. W., Penoncello, S. G. & Lemmon, E. W. Current status of thermodynamic properties of hydrogen. *Int. J. Thermophys.* **28**, 758–772 (2007).
48. Adamczyk, A. J., Reyniers, M.-F., Marin, G. B. & Broadbelt, L. J. Kinetic correlations for H_2 addition and elimination reaction mechanisms during silicon hydride pyrolysis. *Phys. Chem. Chem. Phys.* **12**, 12676–12696 (2010).
49. Pérez, M., Hounjet, L. J., Caputo, C. B., Dobrovetsky, R. & Stephan, D. W. Olefin isomerization and hydrosilylation catalysis by Lewis acidic organofluorophosphonium salts. *J. Am. Chem. Soc.* **135**, 18308–18310 (2013).
50. Jutzi, P., Müller, C., Stammler, A. & Stammler, H.-G. Synthesis, crystal structure, and application of the oxonium acid $[H(OEt_2)_2]^+[B(C_6F_5)_4]^-$. *Organometallics* **19**, 1442–1444 (2000).

Methods

Details of synthetic procedures, spectroscopic characterization, X-ray structure determinations and computations are given in Supplementary Information.

Synthetic methods

All preparations were carried out under an anhydrous N_2 atmosphere using standard Schlenk and glove box techniques. All glassware was oven dried and cooled under vacuum before use. Commercial reagents were purchased from Yuanli Tech., Sigma-Aldrich, Strem or Apollo Scientific and used without further purification unless indicated otherwise. **2** and $[Et_3Si][B(C_6F_5)_4]$ were prepared following the reported procedures[35,51]. All solvents were dried according to standard procedures using either Vacuum Atmospheres Company solvent purification system or distillation from drying agent such as P_2O_5, $LiAlH_4$ and CaH_2, and then storage over molecular sieves (3 Å) followed by degassing via freeze–pump–thaw cycling.

Analytical methods

NMR spectra were recorded at RT using a Bruker AvanceIII 400 MHz spectrometer. Data for ^{1}H NMR are reported as follows: chemical shift (δ ppm), integration, multiplicity (s is singlet, d is doublet; t is triplet, q is quartet, quin is quintet, sep is septet, m is multiplet and br is broad), coupling constant (Hz) and assignment. Gas chromatography–mass spectrometry analyses were obtained on a 7890B gas chromatography system equipped with DB-5ms UI column (30 m × 0.25 mm ID × 0.25 µm film) and 5978A mass selective detector (Agilent Technologies). Elemental analysis was carried out using an Elementar UNICUBE analyser, which was standardized using acetanilide. High-resolution mass spectrometry was performed with a Waters SYNAPT system.

X-ray crystallographic methods

The crystals for all the reported compounds herein were mounted on a cryoloop with paratone oil, and all data were collected at 100(2) or 110(2) (for **1-Cl**) K. Single-crystal X-ray diffraction data for **1-Cl**, **1-OTf** and $[\mathbf{1}^+][\mathbf{B(C_6F_5)_4}]$ were collected on a Bruker KAPPA APEXDuo diffractometer equipped with an APEX II CCD detector using a TRIUMPH monochromator with a MoKα X-ray source (α = 0.71073 Å). Unit cell determination, refinement and data collection were done using the Bruker APEX-III suite[52], data reduction and integration were performed using SAINT v8.34A (Bruker)[53] and absorption corrections and scaling were done using SADABS-2014/5 (Bruker)[54]. Single-crystal X-ray diffraction data for $[\mathbf{1}^+\text{-}\mathbf{H_2}][\mathbf{B(C_6F_5)_4}]$ were collected on a Rigaku Oxford Diffraction–XtaLAB Synergy-S diffractometer operated with monochromated MoKα X-ray source (α = 0.71073 Å) and the data collection, cell refinement, data reduction and analytical method absorption correction were performed using CrysAlis^{Pro}. All the crystal structures were solved through the OLEX2 (ref. 55) package using SHELXT[56] and the structures were refined using SHELXL[57]. All non-hydrogen atoms were refined anisotropically. All the figures were generated using Mercury 3.0.

Computational methods

DFT calculations were performed using Gaussian 09 (ref. 58). Geometry optimization of all the molecules, intermediates and the transition states were carried out using the BP86(D3)/def2-TZVP level of theory[39–43] in $CHCl_3$ using the CPCM model[45,46]. Thermal energy corrections were extracted from the results of frequency analysis performed at the same level of theory. Frequency analysis of all the molecules and intermediates contained no imaginary frequency showing that these are energy minima. The transition states geometries gave one imaginary frequency at expected reaction coordinates confirming that it is a first-order saddle point. The AIM analysis was performed using Multiwfn[59]. The computational pictures were generated using, Avagadro[60] and CYLView[61].

Data availability

The data supporting the findings of this study are available within the paper and its Supplementary Information (experimental procedures, DFT calculations and characterization data). X-ray data are available free of charge from the Cambridge Crystallographic Data Centre under references CCDC-2267545 (**1-Cl**), CCDC-2267548 (**1-OTf**), CCDC-2267547 ($[\mathbf{1}^+][B(C_6F_5)_4]$) and CCDC-2267546 ($[\mathbf{1}^+\text{-}\mathbf{H_2}][B(C_6F_5)_4]$). These data can be obtained free of charge from The Cambridge Crystallographic Data Centre (www.ccdc.cam.ac.uk/data_request/cif). The Cartesian coordinates and energies of all optimized molecules are provided as *.xyz files.

References

51. Connelly, S. J., Kaminsky, W. & Heinekey, D. M. Structure and solution reactivity of (triethylsilylium)triethylsilane cations. *Organometallics* **32**, 7478–7481 (2013).
52. Bruker APEX III. *Bruker AXS Inc.* https://bruker.com/ (2019).
53. Bruker SAINT v8.34A. *Bruker AXS Inc.* https://bruker.com/ (2013).
54. Bruker Sadabs, 2014/5. *Bruker AXS Inc.* https://bruker.com/ (2015).
55. Dolomanov, O. V., Bourhis, L. J., Gildea, R. J., Howard, J. A. K. & Puschmann, H. OLEX2: a complete structure solution, refinement and analysis program. *J. Appl. Crystallogr.* **42**, 339–341 (2009).
56. Sheldrick, G. M. SHELXT - Integrated space-group and crystal-structure determination. *Acta Cryst.* **A71**, 3–8 (2015).
57. Sheldrick, G. M. Crystal structure refinement with SHELXL. *Acta Cryst.* **C71**, 3–8 (2015).
58. Frisch, M. J. et al. Gaussian 09, revision D.01. *Gaussian, Inc.* https://gaussian.com/ (2010).
59. Lu, T. & Chen, F. Multiwfn: a multifunctional wavefunction analyzer. *J. Comput. Chem.* **33**, 580–592 (2012).
60. Hanwell, M. D. et al. Avogadro: an advanced semantic chemical editor, visualization, and analysis platform. *J. Cheminform.* **4**, 1–17 (2012).
61. Legault, C. Y., CYLview20 *Université de Sherbrooke* http://www.cylview.org (2020).

Acknowledgements

This work was supported by the Israeli Science Foundation, grant 195/22, the Israel Ministry of Science Technology & Space, grant 01032376, and the US–Israel Binational Science Foundation, grant 2018221. D.T. thanks the Ariane de Rothschild Women Doctoral scholarship for outstanding female PhD students.

Author contributions

D.B., D.T. and K.J. performed all the synthetic work. D.B. analysed and solved all X-ray molecular structures and did all the computational studies. R.D. supervised the project and wrote the paper with input from all authors.

Competing interests

The authors declare no competing interests.

Additional information

Supplementary information The online version contains supplementary material available at https://doi.org/10.1038/s41557-024-01569-y.

Correspondence and requests for materials should be addressed to Roman Dobrovetsky.

Peer review information *Nature Chemistry* thanks Josh Abbenseth, Shigeyoshi Inoue and the other, anonymous, reviewer for their contribution to the peer review of this work.